International Journal of Nanomedicine

Dovepress
open access to scientific and medical research

Open Access Full Text Article

ORIGINAL RESEARCH

Prostate Cancer Cellular Uptake of Ternary Titanate Nanotubes/$CuFe_2O_4$/Zn-Fe Mixed Metal Oxides Nanocomposite

This article was published in the following Dove Press journal:
International Journal of Nanomedicine

Ahmed AG El-Shahawy[1]
SA Abdel Moaty[2]
AH Zaki[1]
Nada A Mohamed[2]
Yasser GadelHak[1]
RK Mahmoud[2]
AA Farghali[1]

[1]Materials Science and Nanotechnology Department, Faculty of Postgraduate Studies for Advanced Sciences (PSAS), Beni-Suef University, Beni-Suef, Egypt; [2]Chemistry Department, Faculty of Science, Beni-Suef University, Beni-Suef, Egypt

Background: Certainly, there is a demand for stronger recognition of how nanoparticles can move through the cell membrane. Prostate cancer is one of the forcing sources of cancer-relevant deaths among men.

Aim of the Work: The current research studied the power of prostate cancer cells to uptake a ternary nanocomposite TNT/$CuFe_2O_4$/Zn-Fe mixed metal oxides (MMO).

Methodology: The nanocomposite was synthesized by a chemical method and characterized by a High-resolution transmission electron microscope, Field emission scanning electron microscope, X-ray diffraction, Fourier transmission infra-red, X-ray photoelectron spectroscopy, dynamic light scattering. Besides, it was implemented as an inorganic anticancer agent versus Prostate cancer PC-3 cells.

Results: The results revealed cellular uptake validity, cell viability reduction, ultra-structures alterations, morphological changes and membrane damage of PC-3 cells.

Conclusion: The prepared ternary nanocomposite was highly uptake by PC-3 cells and possessed cytotoxicity that was dose and time-dependent. To conclude, the study offered the potential of the investigated ternary nanocomposite as a promising prostate anticancer agent.

Keywords: cytotoxicity, inorganic nanomaterials, prostate cancer

Background

Investigations have indicated that 25% of men are diagnosed with prostate cancer (PCa).[1] The clinical diagnostic approach is testing the prostate-specific antigen (PSA) level, where a concentration > 4 ng/mL is considered a risk of biopsy.[2] The routine diagnostic technique is the digital rectal examination, and Multi-parametric-magnetic resonance imaging allows the potential diagnosis of PCa.[3] The distinct five stages of PCa are (zero) I, II, III, and IV,[4] and most cases of prostate cancer metastasis develop in the lymph nodes and the bones.[5] Choice of the treatment procedure, whatever surgery, radiation, hormone, Cryo-therapy, Vaccine, and Bone-directed treatment depends on the clinical stage, the age, and the general health of the individual.[6]

The potential complications of the mentioned approaches are serious to consider.[7] The prostate size is the fundamental limitation of surgery, and 5 to 20% of cases suffer from stress incontinence after radical prostatectomy. Hormonal therapy leads to loss of libido, bone, and muscle mass.[8] Further, 30 to 50% experience erectile dysfunction after radiation therapy,[9] and urinary retention, urgency, and frequency are more common in Brachytherapy.[10]

Correspondence: Ahmed AG El-Shahawy
Tel +201226798209
Email Ahmedelshahawy382@yahoo.com

submit your manuscript | www.dovepress.com
DovePress
http://doi.org/10.2147/IJN.S228279

Recent improvements in cancer nanomedicine have a significant consideration.[11] In specific, metal and metal oxides inorganic nanoparticles (NPs) are substantial parts in the clinical progress of cancer diagnostic and therapy.[12,13] For instance, Iron oxide NPs in Glioma,[14] Graphite for Prostate,[15] Gold in Cervical,[16] Selenium/Ruthenium/copper for breast,[17] Titanium peroxide with the pancreas, Platinum in the lung[18] and Graphene in Non-small-cell lung carcinoma.[19,20] Further, titanium dioxides TiO_2 NPs have promising anticancer activities towards the breast[21] and prostate.[22,23] Besides, ferrites magnetic inorganic NPs are good anticancer agents, as Zinc,[24,25] Nickel,[26] Zinc-Nickel,[27] Cobalt[28] and super-paramagnetic iron oxide.[29] Besides, the developed NPs target the PCa using aptamer, antibody[30] and prostate-specific membrane antigen surface marker.[31]

However, the major drawback of inorganic NPs is their toxicity, which impairs the proteins, lipids, and DNA of the normal cell.[32] In specific cases, inorganic NPs inhibit the cellular efflux pump by disturbing the Ca^{2+} concentration.[33] So far, the researchers denoted the efficacy of inorganic NPs in cancer therapy, but the main limitation is the only concern at high concentration. Additionally, the issue of cell penetration, translocation and subsequent aggregation inside the cell, or in the cellular compartments is still a critical case.

Lately, nanostructures, such as ternary nanocomposites have potential usage in different fields since synergistic effects of their ingredients at the nanoscale domain may enhance the physical and chemical properties when compared to individual phases,[34] for example, a novel sensitive photo-electrochemical ternary nanocomposite biosensor for glucose detection and sensing.[35,36] Ternary nanocomposite films with different NPs exhibited superior chemical, thermal, mechanical properties, and electrochemical capacitance,[37,38] a biocompatible nanocomposite of silver/gold alloy showed potential anticancer activities against liver cancer.[39]

To limit the cytotoxicity of the individual inorganic nanoparticles at high concentrations, the present research was planned to synthesis a ternary nanocomposite that constituted of titanate nanotubes/cupper ferrite/zinc-iron mixed metal oxides (MMO) (TNT/$CuFe_2O_4$/Zn-Fe MMO), in addition, to investigate how and to what extent the validity of prostate cancer cellular uptake in trial to achieve high efficacy with low concentration as an adequate anticancer inorganic agent versus PCa.

Materials and Methods

Materials

$CuFe_2O_4$ and Zn-Fe layered double hydroxides (LDH) were prepared using nitrate salts, Fe $(NO_3)_3.9H_2O$ (Alpha Chemika, India), Cu $(NO_3)_2.3H_2O$ (Alpha Chemika, India) and Zn $(NO_3)_2.6H_2O$ (Oxford Laboratory Reagent, India). Sodium hydroxide (NaOH) was purchased from Piochem for laboratory chemicals, Egypt, and hydrochloric acid (HCl) was obtained from Carlo Erba reagents. All chemicals were of reagent grade quality and used with no further purification.

Human prostate cancer PC-3 cell lines were obtained from the American-Type Culture Collection (ATCC, Rockville, MD). Mammalian cell lines: MRC-5 cells (Normal human Lung fibroblast cells) were acquired from VACSERA Tissue Culture Unit, Egypt. The used chemicals were Dimethyl sulfoxide (DMSO), MTT and trypan blue dyes were purchased from Sigma (St. Louis, Mo., USA). Fetal Bovine serum, DMEM, RPMI-1640, HEPES buffer solution, L-glutamine, gentamycin and 0.25% Trypsin-EDTA, Osmium tetroxide chemical fixes fat and sodium cacodylate buffer, Uranyl acetate staining, lead citrate phosphate-buffered saline (PBS), acetone, 4% of glutaraldehyde and 10% formalin were procured from Lonza (Belgium). Doxorubicin as a reference standard was taken from Sigma Aldrich.

Preparation of TNT/$CuFe_2O_4$/Zn-Fe MMO

Titanate nanotubes were formed in agreement with our preceding research with minor adjustments.[32] Quickly, 10g of Anatase TiO_2 powder was suspended in 500 mL of 10 M NaOH solution, transferred to a 1000 mL hydrothermal autoclave, and heated at 160°C for 23 hrs. TNT/$CuFe_2O_4$ with a 1:1 ratio was prepared using the co-precipitation approach. In the LDH phase, the molar ratio of Zn/Fe was 4:1.[33] Originally, an aqueous solution of TNT was sonicated for 30 min in 4 M NaOH solution. Solutions of Cu^{2+} and Fe^{3+} were included drop-wise under vigorous stirring until a pH 10. The obtained precipitates were developed for 24 hrs at 70°C, filtered, washed with bi-distilled water several times, dried at 80°C overnight and calcined at 400°C for 2 hrs. To prepare the Zn-Fe MMO, the corresponding Zn-Fe LDH (1:1 by weight) was deposited over the surface of the TNT/$CuFe_2O_4$ phase through the co-precipitation of the corresponding Zn and Fe nitrate salts using sodium hydroxide as a precipitating

agent. After precipitation, the powder was separated by centrifugation, washed several times and left to dry overnight at 40°C. Converting the LDH phase into the corresponding MMO was achieved through heating the dried samples at 200°C and left to cool naturally. Preparing MMO from the corresponding LDH phase is considered as a simple and economical procedure, which allows the MMO to keep the layered morphology of the original LDH phase after being heated.

Material Characterization

The prepared nanocomposite was characterized by high-resolution transmission electron microscopy HRTEM (JEOL-JEM 2100), field emission scanning electron microscopy FESEM (Gemini, 154 Zeiss-Ultra 55, field emission high-resolution scanning electron 155 microscope), X-ray diffraction XRD, X-ray photoelectron spectroscopy XPS (Thermo-Scientific k-Alpha), Zeta sizer and zeta potential (Malvern Instruments Ltd), Fourier transformation infrared spectroscopy FTIR (Vertex 70 FTIR-FT Raman) to study the microstructure, morphology, crystallinity, quantitative elemental composition chemical state, size distribution, surface potential and the functional groups, respectively.

Testing the Cellular Uptake by TEM

The PC-3 cells were shaken well and left intact for 20 hrs, the suspension was centrifuged down to a pellet and rinsed twice with PBS and then the samples were developed adopting standard practices for transmission electron microscopy (TEM), where post-fixation was carried out in 1% osmium tetroxide in cacodylate buffer at room temperature for 1 hr. The cells were dehydrated in acetone and buried in Epon resin. Ultrathin pieces were stained with Uranyl acetate and lead citrate and later probed with a TEM (70 kV GEOL GEM-1010) at the Regional Centre for Mycology and Biotechnology (RCMB), Egypt.

Morphological Analysis

Again, the investigated PC-3 cells were incubated at 37°C for 24 hrs. After that, the cells were soaked with PBS triplicates and were prefixed with 4% of glutaraldehyde solution for overnight and laved three times with 0.1 M sodium cacodylate buffer for 10 mins. The specimens were fixed in 1% of osmium tetroxide at 4oC for 2 hrs and washed plentiful with 0.1 M sodium cacodylate buffer for 10 mins. Subsequently, the specimens were dehydrated with a series of ethanol washes (30, 50, 70, 90, and 100%); critical point dried in CO_2, coated with gold, and examined with a 20 kV JEOL JSM-5500LV Scanning Electron Microscope (SEM) at RCMB.

Viable Cell Counting (Trypan Blue Assay)

The treated PC-3 with the tested nanocomposite cells were separated using 0.25% trypsin for 10 mins, then 0.50 µL of PC-3 cell suspension was placed in a cryo-vial. An equal part of 0.4% trypan blue dye was added to the cell suspension to obtain a 1 to 2 and was mixed by pipetting up and down. The mixture was incubated at room temperature for 2 mins. Later, the cells were counted with an automated cell counter (TC10 Automated Cell Counter 145–0001; Bio-Rad Laboratories, Inc., Hercules, CA, USA). The percentage of viable cells was calculated by dividing the number of viable cells by the number of total cells and multiplying by 100 or % viable cells = [1.00 – (Number of blue cells ÷ Number of total cells)] × 100.[40]

Antitumor Activity Assay

The procedures followed.[41] First, the PC-3 cells were cultivated on RPMI-1640 medium supplemented with 10% inactivated fetal calf serum and 50 µg/mL gentamycin, kept at 37 ºC in a moistened environment with 5% CO_2 and sub-cultured three times a week. For cytotoxicity evaluation using viability assay, the PC-3 cells were suspended in a medium in Corning® 96-well tissue culture plate with a concentration $5x10^4$ cell/well and then incubated for 24 hrs. Second, sequential double-fold dilutions of the tested nanocomposite were included in a 96-well plate (three repeats). Six vehicles with media 0.5% DMSO were run as a control (untreated with the investigated nanocomposite). After incubating for 24 hrs, the numbers of viable cells were detected by the MTT test.

Shortly, the media was expelled from the well plate and recovered with 100 µL of pure culture RPMI 1640 medium, and 10 µL of the 12 mM MTT stock solution (5 mg of MTT in 1 mL of PBS) were added to each well including control and was incubated further at 37°C and 5% CO_2 for 4 hrs. Finally, an 85 µL aliquot of the media was removed from the wells, and 50 µL of DMSO was included to each well and mixed thoroughly with the pipette and incubated at 37°C for 10 mins.

The optical density was measured at 590 nm with the microplate reader (SunRise, TECAN, Inc, USA) to detect the total viable cells. The percent of viability was calculated as [(ODt/ODc)] x100% where ODt is the mean optical density of treated wells and ODc is that of untreated cells.

The experiments and measures were conducted three times, and the results were presented as the average±Standard Deviation. The relationship between tested nanocomposite versus inhibitory and viability percent was plotted in a bar chart using Graphpad Prism software (San Diego, CA. USA), and the 50% inhibitory concentration (IC50), which is the concentration required to cause toxic effects in 50% of intact cells was determined. The cytotoxicity of the tested nanocomposite was assessed against Mammalian cell lines: MRC-5 cells (Normal human Lung fibroblast cells). In addition, the efficacy of the tested nanocomposite was compared with a standard Doxorubicin.

Results and Discussion

Material Characterization

Figure 1A displays the X-ray diffraction (XRD) of the studied nanocomposite. The sharp peaks at 31.89°, 34.5°, 36.3°, 47.61°, 56.6°, 62.9°, and 68° are characteristic peaks for the (100) (002) (101) (102) (110) (103) and (112) planes, respectively, and well matched with (ICDD card number: 01-070-2551). Mild heating of the LDH phase formed the corresponding MMO of ZnO as a dominant phase with the trivalent Fe^{+3} cations those uniformly distributed in the oxide network. $ZnFe_2O_4$ phase was absent; its detection required heating at 600°C.[42] Besides, the peaks at 31.89°, 34.5°, 36.3° and 62.9° reflected the diffraction peaks of the CuF_2O_4 phase (112) (103) (211) and (224) planes, respectively.[43] The diffraction peak of the titanate phase was low intensities compared with the MMO and ferrite phases and could not be observed in the XRD diffractogram. The structure of the nanocomposite is further illustrated in Scheme 1.

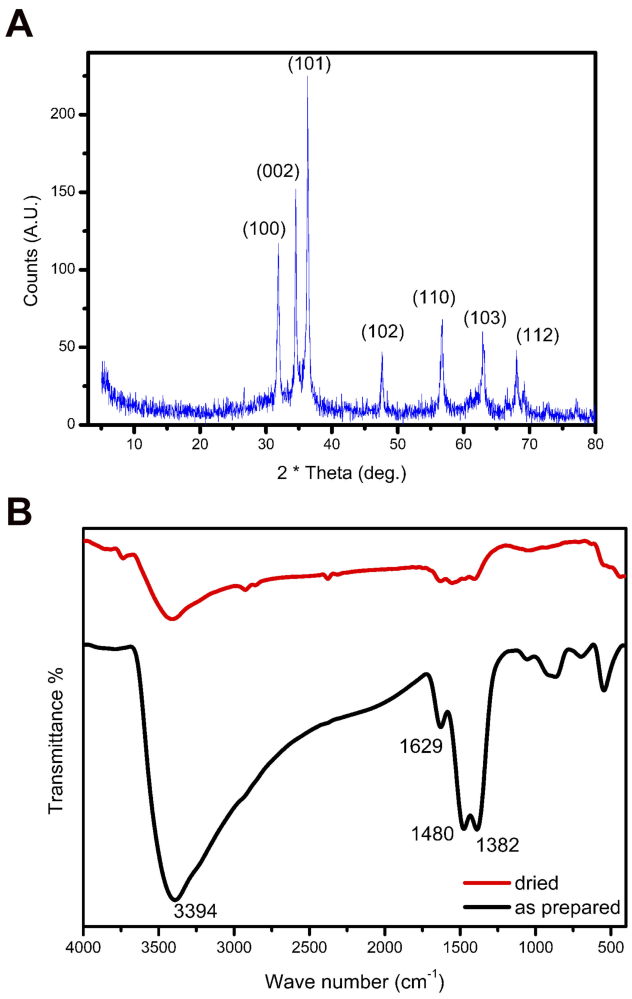

Figure 1 (**A**) XRD pattern of the prepared ternary nanocomposite, (**B**) FTIR pattern of the prepared ternary nanocomposite.

Figure 1B indicates the FTIR range of the synthesized nanocomposite. The absorption peaks at 3394 cm^{-1} and 1629 cm^{-1} illustrates the OH stretching and bending, respectively, because of the adsorbed water molecules[44] while the those at 1382 cm^{-1} and 1480 cm^{-1} assigned to the ν_3 stretching vibration of the NO_3[45] and carbonate[46] groups, and the peaks at the low wave number attributed to the metal-oxygen bond absorption.[47]

X-ray photoelectron spectroscopy was performed to confirm the ingredients elemental composition of the prepared ternary nanocomposite and to determine its oxidation state. Figure 2 presents the XPS spectrum of the inorganic nanomaterials forming the ternary nanocomposite. Overall, XPS results evidenced that all the ingredients were in oxide form rather than in metallic one. The spectrum emphasizes Cu^{+2}, Fe^{+3}, Zn^{+2} and Ti^{+4} originating from the $CuFe_2O_4$, mixed metal oxide (Zn-Fe) and titanate phase, respectively. The Figure clarifies different peaks of various oxidation states at distinct binding energy levels; the peak of Fe 2p was detected at the binding energy 712 and 725 eV confirming the +3 oxidation state of iron and matched with the preceded study.[48] The peaks at 1022.7 and 1044.72 eV attribute to the +2 oxidation state of (ZnO), similar to another research.[49,53] The peak of Cu 2p appears at 932 eV specifies to Cu^{2+} while peaks of Ti 2p assign to Ti^{4+}.[50,54,55]

Figure 3A shows the SEM micrograph of the prepared nanocomposite; two morphologies appeared as a layered morphology of Zn-Fe MMO and fine aggregates that originated from the titanate and ferrite phases. Figure 3B is a TEM image indicating all three phases as titanate nanotubes decorated by $CuFe_2O_4$ and layered Zn-Fe MMO as illustrated in Scheme 1. TNTs have an average diameter ranging between 10–15 nm. Figure 3C reveals the formed-walls of the TNTs.

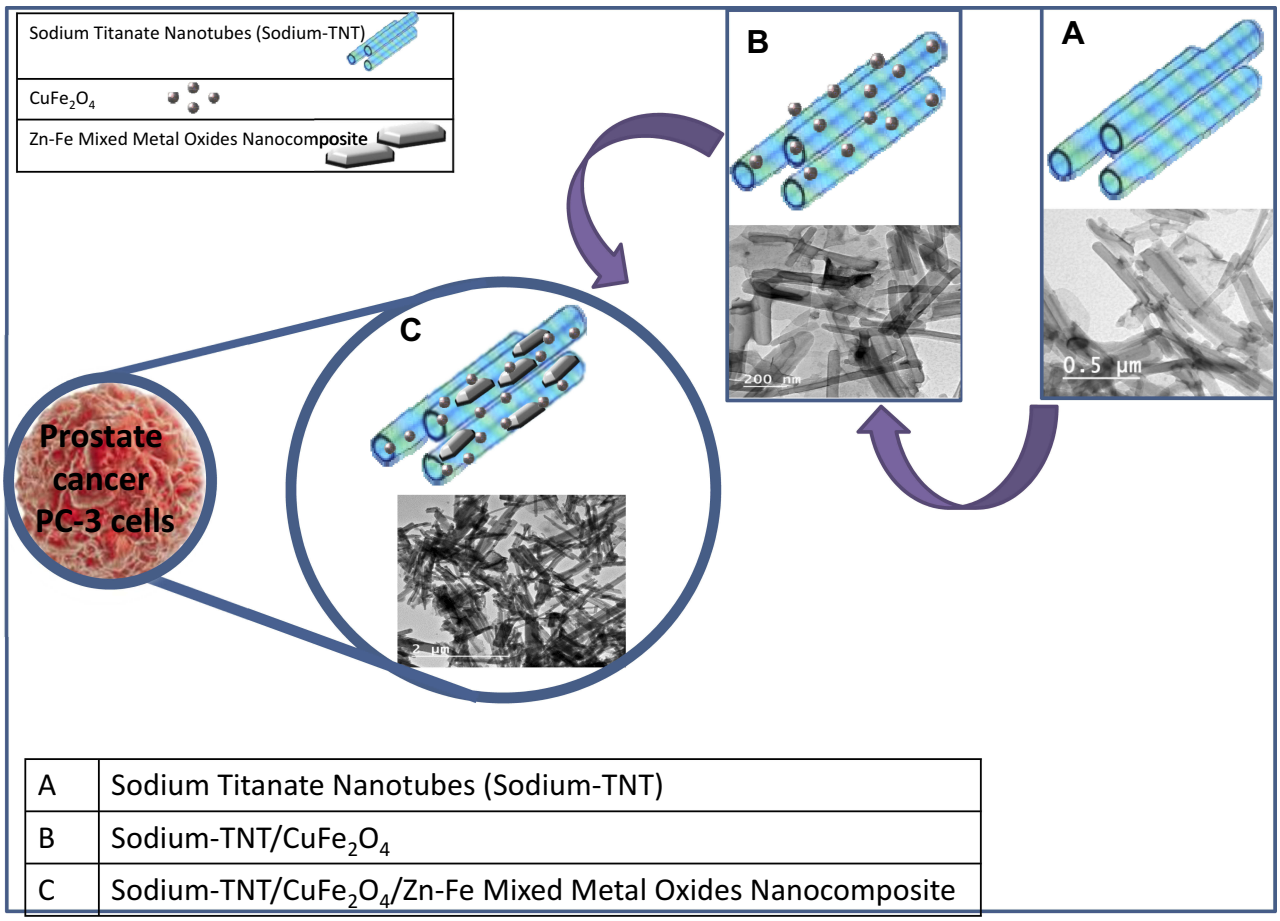

A	Sodium Titanate Nanotubes (Sodium-TNT)
B	Sodium-TNT/$CuFe_2O_4$
C	Sodium-TNT/$CuFe_2O_4$/Zn-Fe Mixed Metal Oxides Nanocomposite

Scheme 1 Possible structure of the ternary nanocomposite.

In the inset image (selected area electron diffraction SAED), the bright spots confirmed an accepted crystallinity of the TNTs phase. Figure 3B displays a hexagonal symmetry of the MMO layers with an edge-to-edge distance of 60 nm. Figure 3D shows fine and well-dispersed $CuFe_2O_4$ spheres with diameters less than 10 nm, and inset reflected a good crystallinity of the ferrite phase.

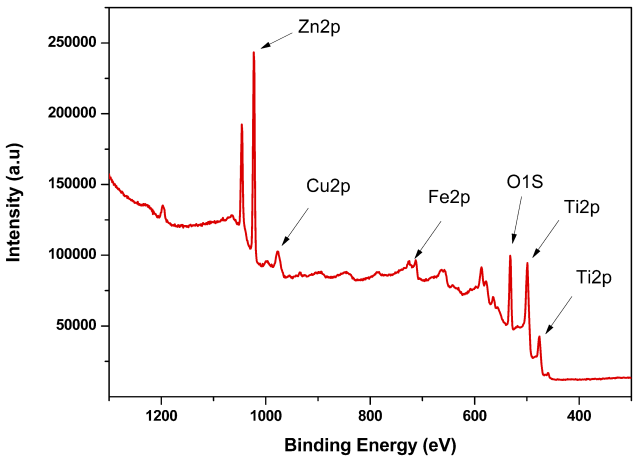

Figure 2 XPS spectrum of titanate nanotubes/$CuFe_2O_4$/Zn-Fe MMO.

Figure 4 reveals the hydrodynamic size distribution of the prepared nanocomposite and showed two peaks at 117.7 nm and 557.4 nm, which attributed to the aggregates and layered morphologies, respectively. The reported poly distribution index PDI was 0.54 that reflected the heterogeneous distribution of the tested nanocomposite, as expected. The particles' tendency to form aggregates or dispersed depends on the surface charge; the calculated zeta potential was −26.4 mV indicating incipient stability.

Cellular Uptake

Indeed, the cellular entry of nanoparticles and their ulterior interaction with the cell's internal structure, together with the power to envisage cultures of nanoparticles at high resolution within cells is a crucial point to infer the processes of any toxicity. It has evidenced that the imaging-based devices are

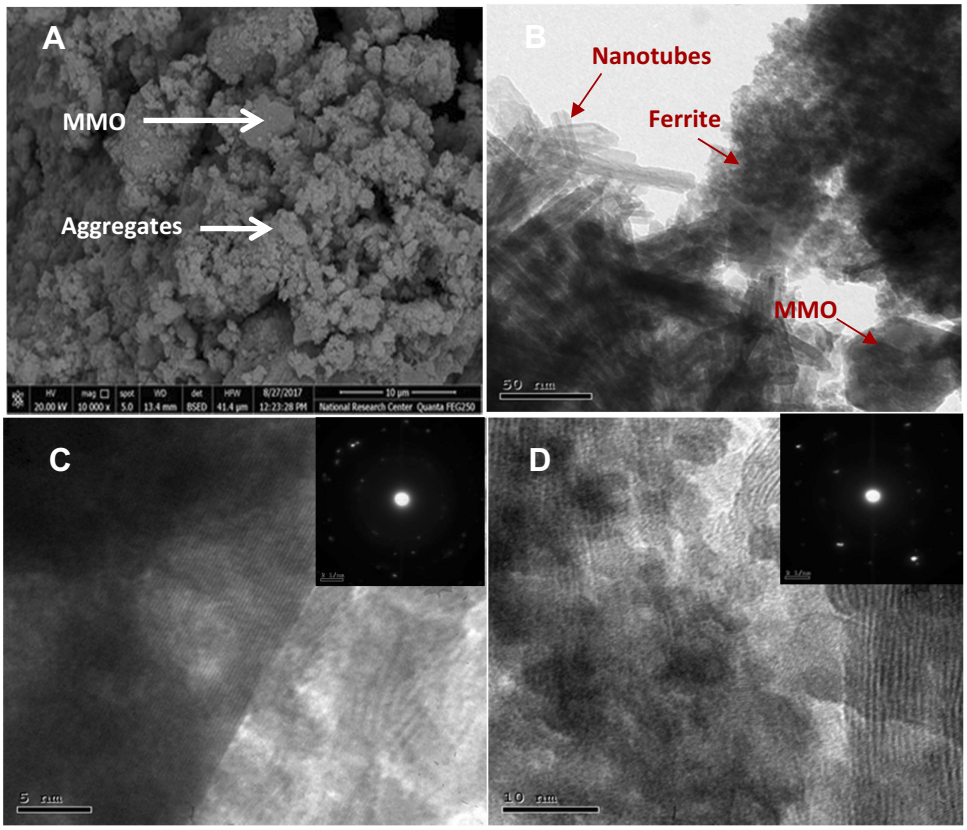

Figure 3 (**A**) FESEM and (**B**) TEM micrographs of the prepared nanocomposite. (**C**) HRTEM micrograph of the TNTs phase (inset: SAED pattern) and (**D**) HRTEM image of the ferrite phase (inset: SAED pattern).

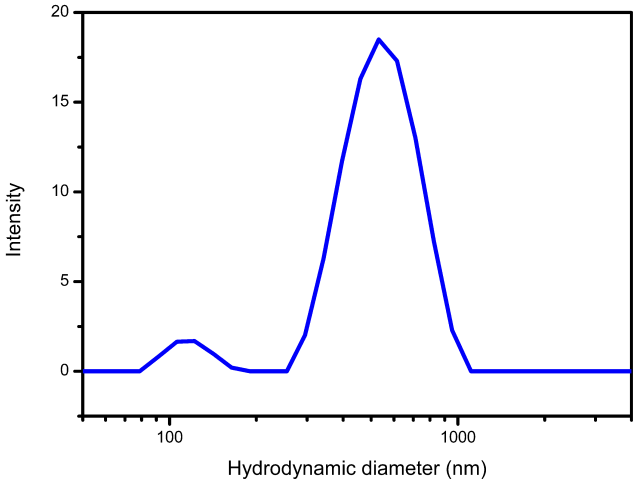

Figure 4 Hydrodynamic size distribution of the prepared ternary nanocomposite.

worthy of investigating the nanoparticle-cell actions; the current study used electron-based imaging techniques to recognize the cellular uptake of the investigated nanocomposite.

Figure 5 gives information about two different TEM images of the prostate cancer cells after incubation with the tested nanocomposite at two distinct times (a) after 24 hrs and (b) after 48 hrs. The figure proves a variation nanocomposite distribution in the extracellular and intracellular matrix, as well as in the degree of the cellular uptake. The image of Figure 5 (a) displays a lot of vacuoles and the distributed nanocomposite in the extracellular regions, also, external attachment to the cell membrane, and dissemination of the nanoparticles in the cytoplasm.

Determining the entrance mechanism is paramount; when NPs come to the surface membrane of a cell, they can connect with its ingredients or extracellular matrix, and penetrate the cell through endocytosis. Five main precise processes of endocytosis are phagocytosis, clathrin-mediated endocytosis (CME), caveolin-mediated endocytosis, clathrin/caveolae-independent endocytosis, and macropinocytosis.

Based on the theory of each method; the entrance pathway of the studied nanocomposite into the cells may be through Phagocytosis or CME. The first approach was not expected for reasons; Phagocytosis exists primarily in professional phagocytes as macrophages, monocytes, neutrophils, and dendritic cells that were nonexistent in the incubation media. In addition, Phagocytosis of NPs is mostly initiated by the Opsonization process, where

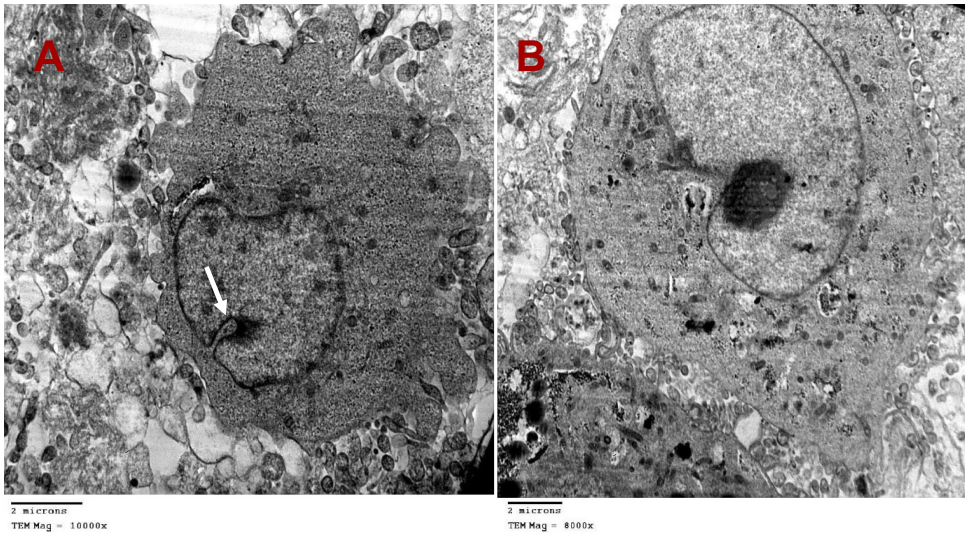

Figure 5 Different TEM images of the PC-3 cells after incubation with the tested nanocomposite materials (IC50 = 29.8 ± 0.6 µg/mL), (**A**) after 24 hrs at 10,000× magnification, (**B**) after 48 h at 8000× magnification.

opsonins such as immunoglobulins, complement proteins, and other blood proteins are adsorbed onto the NPs' surface;[51] these opsonins did not exist also. Further, larger micro-particles experience more efficient uptake by phagocytes while the tested composite was in nano-dimension.

Concerning the second approach, Clathrin-mediated endocytosis occurs either via receptor-specific uptake or by non-specific adsorptive uptake, which is referred to as receptor-independent CME. In receptor-independent CME, the uptake takes place without direct binding with membrane constituents through non-specific hydrophobic molecules or electrostatic interactions that initiate the uptake.

It is important to bear in mind that the surface charge has a powerful effect on the receptor-independent CME uptake mechanism and intracellular fate. For example, anionic particles showed cellular uptake in HeLa cervical cancer cells and silica nanotubes (SNTs).[51] Taken into consideration the surface charge, the prepared nanocomposite bore negative charges that indicated by the zeta potential value. And as such, the suggested entrance mechanism was through electrostatic interaction between $CuFe_2O_4$/Zn-Fe and the phosphate group of the cell membrane lipid layers that caused disruption of the cell membrane integrity, created pores that boosted the entrance of TNT, and developed a tight pit on the inner surface of the plasma membrane; this pit then buds into the cell to complete a covered vesicle in the cytoplasm. The white arrow in Figure 5 illustrated the coated pits and vesicles budding in the cell's cytoplasm, these covered pits and vesicles budding developed steadily by time after 48 hrs of incubation as presented in Figure 5B, which in turn reflected that the distributed nanocomposite in the cytoplasm indented to accumulate around the nuclear membrane, and it needed more 48 hrs of incubation to invade the nuclear envelope. In light of forgoing, the receptor-independent CME mode was the suggested mechanism of invasion and cellular uptake.

Cellular Morphological Changes

Figure 6 provides three TEM images (a, b &c) after 48 hrs of incubation. Overall, it confirmed factual details of the ultra-structural reforms of the PC-3 cells. For example, Figure 6A exhibits a heap of the nanocomposite at the internal wall of the cell membrane face to the cytoplasm. Additionally, the figure represented an alteration of the cell shape and the cell membrane with a slight elongation of the cell. This protraction increased gradually by time as confirmed in Figure 6B, and the piles of the nanocomposite still spread in the cytoplasm. Moreover, Figure 6C illustrates a sinuosity of the cell membrane; this tortuosity may increase the permeability of the membrane. Increasing permeability occurs in the cells that passed the death mechanism whatever by apoptosis or necrosis. The turban blue sassy emphasized the increased permeability. Further, the cytoplasm appeared clear in Figure 6C, reflecting the effect of the nanocomposite on the different organelles in the cytoplasm.

Although the TEM reveals the intracellular distribution of the nanomaterial; nevertheless, but the quantification of the internalized nanomaterials is of fundamental concern.

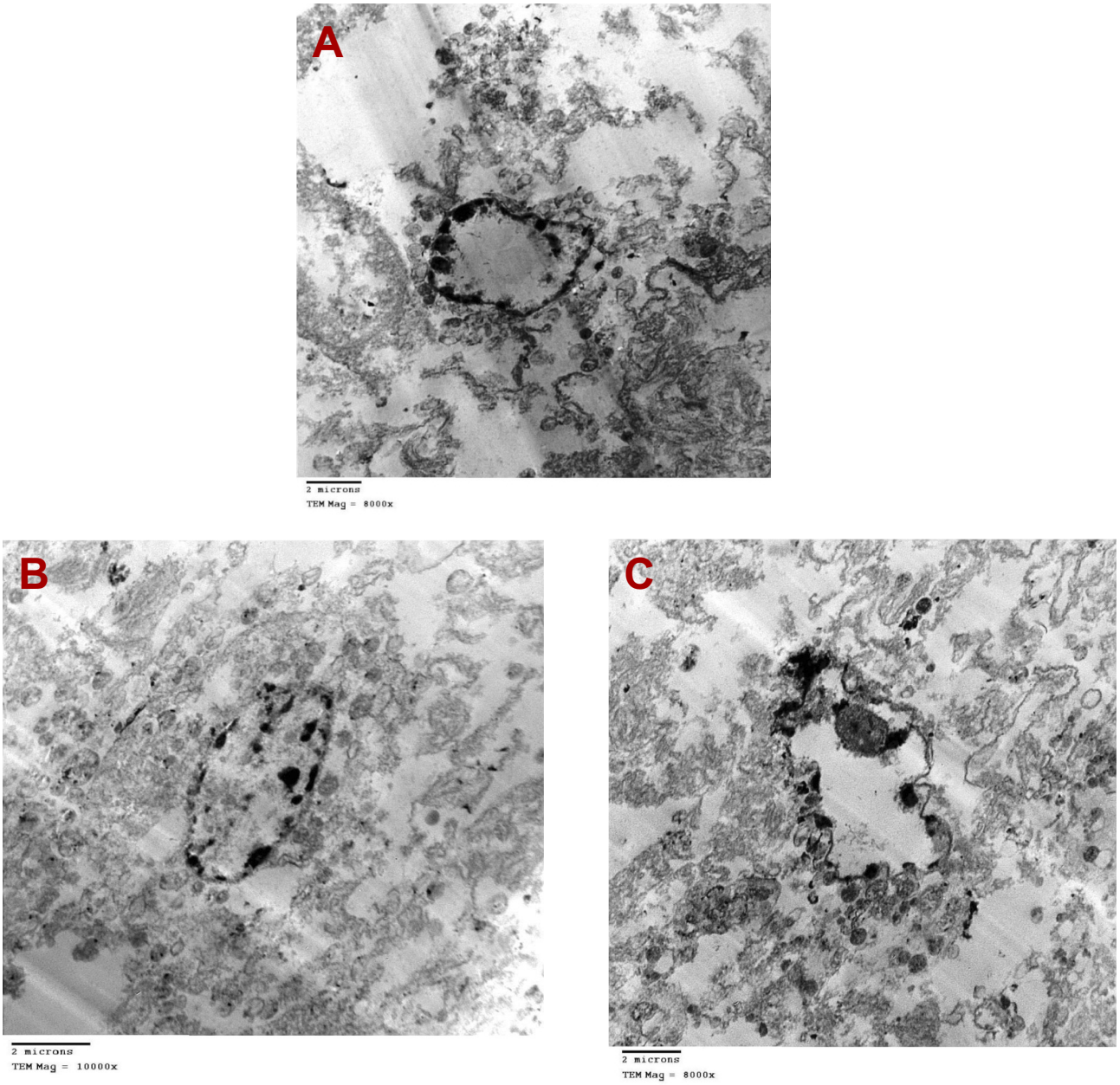

Figure 6 Accurate details of the ultra-structural changes of the PC-3 treated cells with the tested nanocomposites materials (IC50 = 29.8 ± 0.6 µg/mL) after 48 hrs of incubation, (**A**) at 8000× magnification, (**B**) at 10,000× magnification and (**C**) at 8000× magnification.

Up to date, there is no standardized and validated method available for this specific question because of different needs of the analytical methods depend on the particle type, the biological environment as well as the various specifications and limitations for each of the techniques.

Ultimately, Figure 7 reviews four SEM images of the PC-3 cells (a, b, c & d) with different magnifications, where (a & b) without nanocomposite incubation, while (c &d) with incubation. Overall, Figure 7 describes the morphological alterations provoked by the tested nanocomposite on the PC-3 cells. Figure 7A with a large field of view paraded clusters of well-united and condensed PC-3, and revealed non-consistency grid of collagen fibers that reinforced the PC-3 cells and have a substantial part in prostate growth management. On the other hand, Figure 7B with a small and focused field of view exhibited PC-3 cells with a precise and uniform shape with a distinct cytoplasm.

Regarding the treated PC-3 cells, the image of 7C exhibited a concise cytoplasm (white arrow). Moreover, Figure 7D manifests separate cells and cracker structures, leaving wide cell-free zones that illustrated in the figure as large dark signal intensity spaces (white arrows). In addition, it

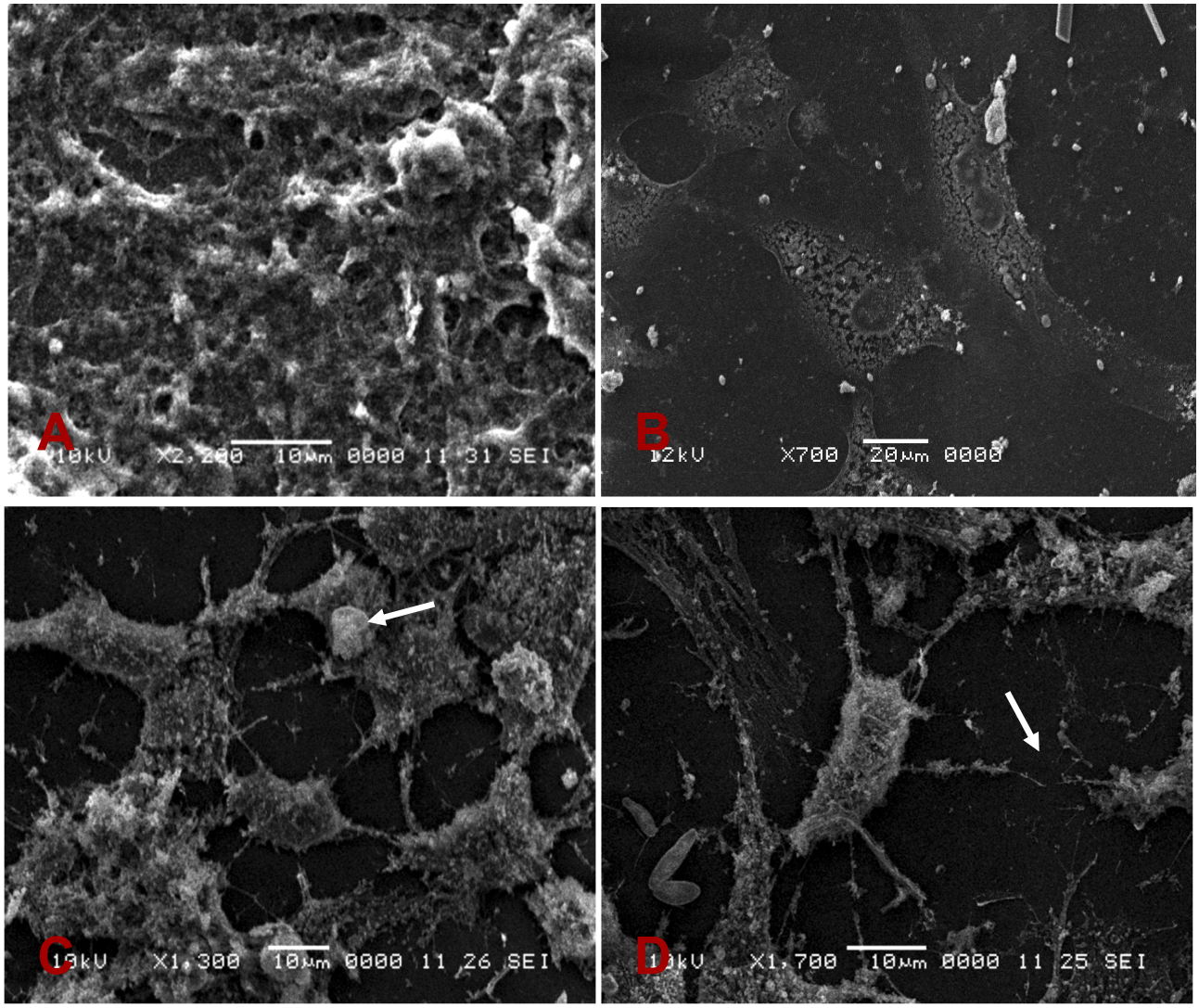

Figure 7 SEM images identify possible morphological alterations caused by the tested nanomaterials on the PC-3 cells. The white arrows refer to a concise cytoplasm and a wide cell-free zone of the treated PC-3 cells.

showed a non-uniform swelling with a fall of fragmentation of collagen tissue, in contrast, the collagen network was intensive with an increased number of fibers in non-treated PC-3 cells, as shown in Figure 7A. It is conceivable that a fraction of the proteins of the connective tissue was ruined during the incubation with the questioned nanocomposite. The morphological analysis by SEM proved variations in the basic connective tissue Stroma (which represents the principal component comprising 54% of the prostate gland), including swelling, fragmentation, and loss of collagen. The presented results were well matched with preceded study.[52]

Cytotoxic Assay

To confirm the implication of the inward nanocomposite; the cytotoxic effect of the tested nanocomposite versus PC-3 was investigated by the Trypan Blue dye exclusion test, which is used to determine the number of viable cells present in a cell suspension. The test is based on the principle that living cells possess intact cell membranes that exclude Trypan Blue dye, whereas Trypan Blue stain can pass through only permeable membranes of the deceased cells, altering their color into blue, which is noticeable under optical microscopy. The treated PC-3 cell suspension with the nanocomposite was mixed with the Trypan Blue dye and visually examined to determine whether cells take up or exclude dye. The cytoplasm of the treated PC-3 cells was stained by blue color while that of viable cells was clear. Overall, the incubated cell lines with the medium involving the ternary nanocomposite showed a substantial rebate in the number of viable cell contrast to the control group ($p<0.05$).

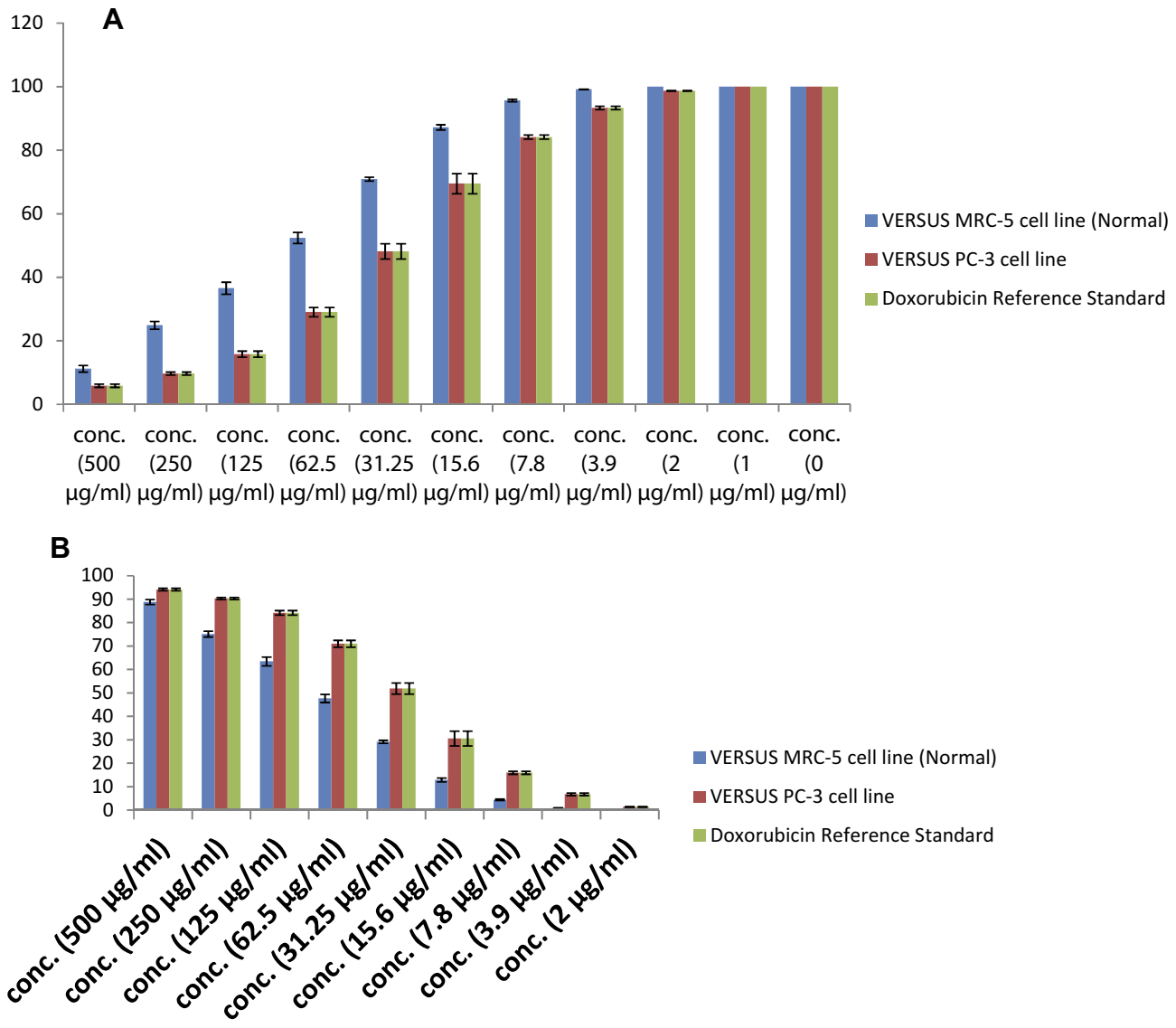

Figure 8 The statistical analysis of the MTT assay, (**A**) the viability and (**B**) inhibitory percent of the PC-3 and MRC-5 cell line (Normal) cells treated by ternary nanocomposites and standard chemotherapy agent (Doxorubicin).

Further, Figure 8 illustrates the statistical analysis bar chart of the MTT assay measurements. Figure 8A shows the viability percent (vertical axis) of the PC-3 and MRC-5 cell line (Normal) versus the tested nanocomposite and a standard chemotherapy agent (Doxorubicin) with serial dilutions (horizontal axis). The viability percent was measured for each concentration, and the data were reported as an average ± Standard Deviation. Overall, the viability percent of the treated cells (PC-3 and MRC-5) decreased with the increase of the concentration. The lowest percent was at the maximum concentration (500ug/mL). It was below 5% of Doxorubicin and closed to 5% of the nanocomposite while the viability of the normal cells was approximately 10%. The viability of the treated PC-3 by Doxorubicin reduced rapidly while those treated by the ternary nanocomposite lessened consistently at low concentration and suddenly diminished at high concentration. The cytotoxic effect of the nanocomposite on the normal MRC-5 appeared obviously at high concentrations. On the other hand, Figure 8B is a chart clarifies the inhibitory percent of the treated cell at the same concentrations, the IC_{50}% of the nanocomposite against PC-3 and MRC-5 was 29.8 ± 0.6 µg/mL and 71.9 ± 2.5 µg/mL, respectively, while IC_{50}% of Doxorubicin versus PC-3 was 3.68 ± 0.2 µg/mL.

The future work of the current research will focus on twofold: performing other assays to indicate the efficiency of the tested ternary nanocomposite against specific

organelles of the PC-3 cells to scout the toxicity pathways, to study the alteration in the hormonal order, to investigate special growth factors and activity of specific enzymes that affects the regulation of the PC-3 growth, and to rebate the main ingredient of the ternary nanocomposite that activate the cytotoxicity of the PC-3 cells meticulously.

To conclude, the safe treatment of inorganic NPs persists a crucial question, and many warrants are still recommended. Furthermore, recognizing the interactions of NPs with cells and how the entrance influences their cellular uptake is essential. Consequently, to limit the cytotoxicity of the individual NPs at high concentrations; the current study presented the ternary nanocomposite TNT/$CuFe_2O_4$/Zn-Fe MMO, investigated the cellular uptake versus PC-3, proposed the receptor-independent CME as an entrance mechanism, showed the intracellular distribution of the tested nanocomposite, reported a distinct alteration in the morphology and ultrastructure of the PC-3, as well as a potential toxicity of the tested ternary nanocomposite that was dose and time-dependent, which reflected a high cellular uptake. In the final, the current study suggests the capability of the tested ternary nanocomposite as a promising prostate anticancer agent.

Abbreviations

PCa, Prostate Cancer; MMO, Mixed Metal Oxides; LDH, Layered double hydroxide; PSA, Prostate-Specific Antigen; DRE, Digital Rectal Examination; mp-MRI, Multiparametric-magnetic resonance imaging; PSMA, Prostate-Specific Membrane Antigen; M6PR, Mannose 6-phosphate receptor; DTX, Docetaxel; TPGS, Tocopheryl polyethylene glycol succinate; CUR, DTX-curcumin; NPs, Nanoparticles; DNA, Deoxyribonucleic acid; DMSO, Dimethyl sulfoxide; PBS, Phosphate Buffered Saline; TNT, Titanate nanotubes; FESEM, Field Emission Scanning Electron Microscopy; IC50, Inhibitory concentration; TEM, Transmission Electron Microscopy; RCMB, Regional Centre for Mycology and Biotechnology; SEM, Scanning Electron Microscope; XRD, X ray Diffraction; FTIR, Fourier transformation infra-red; SAED, Selected Area Electron Diffraction; ROS, Reactive Oxygen Species.

Ethics Approval and Consent to Participate

The authors followed the ethics of research, approved and consented to participate in this study.

Consent for Publication

The authors consent this manuscript for publication.

Data Sharing Statement

The authors emphasize the availability of data and materials.

Acknowledgments

The authors are thankful to all members at Materials Science and Nanotechnology Dept., Faculty of Postgraduate Studies for Advanced Sciences (PSAS), Beni-Suef University Egypt for supporting preparation of the nanomaterials. Also, all members at Central Lab for Characterization and Statistical unite at 57357 Children Cancer Hospital, Egypt.

Author Contributions

Dr. Elshahawy conceived the idea for biomedical application, Dr. A.H. Zaki, Dr. Nada A. Mohamed, Dr. Yasser GadelHak, Dr. S. A. Abdelmoaty Dr. R.K. Mahmoud, and Dr. A A Farghali participated in the study design. Dr. Elshahawy conducted the bio-section, analyzed and interpreted the data. Dr. A.H. Zaki, Dr, Dr. S. A. Abdelmoaty, Dr. R.K. Mahmoud and Dr. A A Farghali prepared the materials. Dr. Yasser GadelHak investigated and Nada A. Mohamed and Dr. R.K. Mahmoud characterized the prepared materials. The authors wrote and revised the manuscript. All the authors approved the final version to be published, and agreed to be accountable for all aspects of the work in ensuring that questions related to the accuracy or integrity of any part of the work are appropriately investigated and resolved.

Disclosure

The authors confirm no competing interests in this work.

References

1. Thompson B, Khan S. Aging men and prostate cancer. *J Reproduktionsmedizin und Endokrinol Reprod Med Endocrinol*. 2016;12:396–398.
2. Adhyam M, Gupta AK. A review on the clinical utility of PSA in cancer prostate. *Indian J Surg Oncol*. 2012;3:120–129. doi:10.1007/s13193-012-0142-6
3. Sidhu HS, Benigno S, Ganeshan B, et al. Textural analysis of multiparametric MRI detects transition zone prostate cancer. *Eur Radiol*. 2017;27:2348–2358. doi:10.1007/s00330-016-4579-9
4. Patel KM, Gnanapragasam VJ. Novel concepts for risk stratification in prostate cancer. *J Clin Urol*. 2016;9:18–23. doi:10.1177/2051415816673502
5. Chen CP, Roach M, Kased N, et al. Management of prostate cancer patients with lymph node involvement: a rapidly evolving paradigm. *Cancer Treat Rev*. 2012;38:956–967. doi:10.1016/j.ctrv.2012.05.005
6. Lakshmanan V-K. Therapeutic efficacy of nanomedicines for prostate cancer: an update. *Investig Clin Urol*. 2016;57:21–29. doi:10.4111/icu.2016.57.1.21
7. Chen Z, Penet M-F, Nimmagadda S, et al. PSMA-targeted theranostic nanoplex for prostate cancer therapy. *ACS Nano*. 2012;6:7752–7762. doi:10.1021/nn301725w

8. Saad F, Aversa A, Isidori AM, et al. Onset of effects of testosterone treatment and time span until maximum effects are achieved. *Eur J Endocrinol*. 2011;165:675–685. doi:10.1530/EJE-11-0221
9. Pettus JA, Masterson T, Sokol A, et al. Prostate size is associated with surgical difficulty but not functional outcome at 1 year after radical prostatectomy. *J Urol*. 2009;182:949–955. doi:10.1016/j.juro.2009.05.029
10. Kragelj B. Obstructive urination problems after high-dose-rate brachytherapy boost treatment for prostate cancer are avoidable. *Radiol Oncol*. 2016;50:94–103. doi:10.1515/raon-2015-0010
11. Shi J, Kantoff PW, Wooster R, Farokhzad OC. Cancer nanomedicine: progress, challenges and opportunities. *Nat Rev Cancer*. 2017;17:20. doi:10.1038/nrc.2016.108
12. Jiao M, Zhang P, Meng J, et al. Recent advancements in biocompatible inorganic nanoparticles towards biomedical applications. *Biomater Sci*. 2018;6:726–745. doi:10.1039/C7BM01020F
13. Bhattacharyya S, Kudgus RA, Bhattacharya R, Mukherjee P. Inorganic nanoparticles in cancer therapy. *Pharm Res*. 2011;28:237–259. doi:10.1007/s11095-010-0318-0
14. Silva AC, Oliveira TR, Mamani JB, et al. Application of hyperthermia induced by superparamagnetic iron oxide nanoparticles in glioma treatment. *Int J Nanomedicine*. 2011;6:591–603. doi:10.2147/IJN.S14737
15. Ishikawa H, Tsuji H, Kamada T, et al. Carbon ion radiation therapy for prostate cancer. *Int J Urol*. 2012;19:296–305. doi:10.1111/iju.2012.19.issue-4
16. Daduang J, Palasap A, Daduang S, et al. Gallic acid enhancement of gold nanoparticle anticancer activity in cervical cancer cells. *Asian Pac J Cancer Prev*. 2015;16:169–174. doi:10.7314/APJCP.2015.16.1.169
17. Liao W, Yu Z, Lin Z, et al. Biofunctionalization of selenium nanoparticle with dictyophora indusiata polysaccharide and its antiproliferative activity through death-receptor and mitochondria-mediated apoptotic pathways. *Sci Rep*. 2015;5:18629. doi:10.1038/srep18629
18. Nakayama M, Sasaki R, Ogino C, et al. Titanium peroxide nanoparticles enhanced cytotoxic effects of X-ray irradiation against pancreatic cancer model through reactive oxygen species generation in vitro and in vivo. *Radiat Oncol*. 2016;11:91. doi:10.1186/s13014-016-0666-y
19. Patel SC, Lee S, Lalwani G, et al. Graphene-based platforms for cancer therapeutics. *Ther Deliv*. 2016;7:101–116. doi:10.4155/tde.15.93
20. Akhtar MJ, Ahamed M, Alhadlaq HA. Therapeutic targets in the selective killing of cancer cells by nanomaterials. *Clin Chim Acta*. 2017;469:53–62. doi:10.1016/j.cca.2017.03.020
21. Sree Latha T, Reddy MC, Muthukonda SV, et al. In vitro and in vivo evaluation of anti-cancer activity: shape-dependent properties of TiO2nanostructures. *Mater Sci Eng C*. 2017;78:969–977. doi:10.1016/j.msec.2017.04.011
22. Thurn KT, Arora H, Paunesku T, et al. Endocytosis of titanium dioxide nanoparticles in prostate cancer PC-3M cells. *Nanomed Nanotechnol Biol Med*. 2011;7:123–130. doi:10.1016/j.nano.2010.09.004
23. Thevenot P, Cho J, Wavhal D, et al. Surface chemistry influences cancer killing effect of TiO2 nanoparticles. *Nanomed Nanotechnol Biol Med*. 2008;4:226–236. doi:10.1016/j.nano.2008.04.001
24. Mohammed L, Gomaa HG, Ragab D, Zhu J. Magnetic nanoparticles for environmental and biomedical applications: a review. *Particuology*. 2017;30:1–14. doi:10.1016/j.partic.2016.06.001
25. Pan UN, Sanpui P, Paul A, Chattopadhyay A. Surface complexed-zinc ferrite magnetofluorescent nanoparticles for killing cancer cells and single particle level cellular imaging. *ACS Appl Nano Mater*. 2018;1:2496–2502. doi:10.1021/acsanm.8b00545
26. Sun L, Xie S, Qi J, et al. Cell-permeable, MMP-2 activatable, nickel ferrite and his-tagged fusion protein self-assembled fluorescent nanoprobe for tumor magnetic-targeting and imaging. *ACS Appl Mater Interfaces*. 2017;9:39209–39222. doi:10.1021/acsami.7b12918
27. Al-Qubaisi MS, Rasedee A, Flaifel MH, et al. Cytotoxicity of nickel zinc ferrite nanoparticles on cancer cells of epithelial origin. *Int J Nanomedicine*. 2013;8:2497. doi:10.2147/IJN.S42367
28. Lojk J, Bregar VB, Strojan K, et al. Increased endocytosis of magnetic nanoparticles into cancerous urothelial cells versus normal urothelial cells. *Histochem Cell Biol*. 2018;149:45–59. doi:10.1007/s00418-017-1605-1
29. Ding C, Wu K, Wang W, et al. Synthesis of a cell penetrating peptide modified superparamagnetic iron oxide and MRI detection of bladder cancer. *Oncotarget*. 2016;8:4718–4729. doi:10.18632/oncotarget.13578
30. Friedman D, Claypool, S AE, Liu R. The smart targeting of nanoparticles. *Curr Pharm Des*. 2013;19:6315–6329. doi:10.2174/13816128113199990375
31. Lee SS, Roche PJ, Giannopoulos PN, et al. Prostate-specific membrane antigen–directed nanoparticle targeting for extreme nearfield ablation of prostate cancer cells. *Tumour Biol*. 2017;39:101042831769594. doi:10.1177/1010428317695943
32. Zaki AM, Zaki AH, Farghali AA, Abdel-Rahim EF. Sodium titanate-bacillus as a new nanopesticide for cotton leaf-worm. *J Pure Appl Microbiol*. 2017;11:725–733. doi:10.22207/JPAM.11.2.11
33. Moaty SAA, Farghali AA, Moussa M, Khaled R. Remediation of waste water by Co–Fe layered double hydroxide and its catalytic activity. *J Taiwan Inst Chem Eng*. 2017;71:441–453. doi:10.1016/j.jtice.2016.12.001
34. Ali A, Ahmed S. A review on chitosan and its nanocomposites in drug delivery. *Int J Biol Macromol*. 2018;109:273–286. doi:10.1016/j.ijbiomac.2017.12.078
35. Wang Y, Bai L, Wang Y, et al. Ternary nanocomposites of Au/CuS/TiO 2 for an ultrasensitive photoelectrochemical non-enzymatic glucose sensor. *Analyst*. 2018;143:1699–1704. doi:10.1039/C8AN00187A
36. Silva CHB, Iliut M, Muryn C, et al. Ternary nanocomposites of reduced graphene oxide, polyaniline and hexaniobate: hierarchical architecture and high polaron formation. *Beilstein J Nanotechnol*. 2018;9:2936–2946. doi:10.3762/bjnano.9.272
37. Kumar SV, George J, Sajeevkumar VA. PVA based ternary nanocomposites with enhanced properties prepared by using a combination of rice starch nanocrystals and silver nanoparticles. *J Polym Environ*. 2018;26:3117–3127. doi:10.1007/s10924-018-1200-0
38. Zhang R, Liao Y, Ye S, et al. Novel ternary nanocomposites of MWCNTs/PANI/MoS 2: preparation, characterization and enhanced electrochemical capacitance. *R Soc Open Sci*. 2018;5:171365. doi:10.1098/rsos.171365
39. Shanmugasundaram T, Radhakrishnan M, Gopikrishnan V, et al. Biocompatible silver, gold and silver/gold alloy nanoparticles for enhanced cancer therapy: in vitro and in vivo perspectives. *Nanoscale*. 2017;9:16773–16790. doi:10.1039/C7NR04979J
40. Basso FG, Pansani TN, Oliveira CFD, et al. Cytotoxic effects of zoledronic acid on human epithelial cells and gingival fibroblasts. *Braz Dent J*. 2013;24:551–558. doi:10.1590/0103-6440201302229
41. Gomha SM, Riyadh SM, Mahmmoud EA, Elaasser MM. Synthesis and anticancer activities of thiazoles, 1, 3-thiazines, and thiazolidine using chitosan-grafted-poly (vinylpyridine) as basic catalyst. *Heterocycl Int J Rev Commun Heterocycl Chem*. 2015;91:1227–1243.
42. Di G, Zhu Z, Zhang H, et al. Simultaneous removal of several pharmaceuticals and arsenic on Zn-Fe mixed metal oxides: combination of photocatalysis and adsorption. *Chem Eng J*. 2017;328:141–151. doi:10.1016/j.cej.2017.06.112
43. Ahmed MA, Okasha N, Mansour SF, El-Dek SI. Bi-modal improvement of the physico-chemical characteristics of PEG and MFe2O4 subnanoferrite. *J Alloys Compd*. 2010;496:345–350. doi:10.1016/j.jallcom.2010.02.009
44. Zhang Q, Zhang T, Wei Y, et al. Removing structural water from sodium titanate anodes towards barrier-free ion diffusion for sodium ion batteries. *J Mater Chem A*. 2017;5:18691–18697. doi:10.1039/C7TA05217K
45. Moaty SAA, Farghali AA, Khaled R. Preparation, characterization and antimicrobial applications of Zn-Fe LDH against MRSA. *Mater Sci Eng C*. 2016;68:184–193. doi:10.1016/j.msec.2016.05.110

46. Jobbágy M, Blesa MA, Regazzoni AE. Homogeneous precipitation of layered Ni (II)– Cr (III) double hydroxides. *J Colloid Interface Sci*. 2007;309:72–77. doi:10.1016/j.jcis.2007.01.010
47. Lu H, Zhu Z, Zhang H, et al. Simultaneous removal of arsenate and antimonate in simulated and practical water samples by adsorption onto Zn/Fe layered double hydroxide. *Chem Eng J*. 2015;276:365–375. doi:10.1016/j.cej.2015.04.095
48. Yamashita T, Hayes P. Analysis of XPS spectra of Fe2+ and Fe3+ ions in oxide materials. *Appl Surf Sci*. 2008;254:2441–2449. doi:10.1016/j.apsusc.2007.09.063
49. Wagner CD, Riggs WM, Davis LE, Moulder JF, Muilenberg GE. *Handbook of X-Ray Photoelectron Spectroscopy*. Eden Prairie, MN: Perkin-Elmer Corp; 1979:38.
50. Pineda M, Fierro JG, Palacios J, et al. Characterization of zinc oxide and zinc ferrite doped with Ti or Cu as sorbents for hot gas desulphurization. *Appl Surf Sci*. 1997;119:1–10. doi:10.1016/S0169-4332(97)00183-9
51. Pašukonienė V, Mlynska A, Steponkienė S, et al. Accumulation and biological effects of cobalt ferrite nanoparticles in human pancreatic and ovarian cancer cells. *Medicina (B Aires)*. 2014;50:237–244. doi:10.1016/j.medici.2014.09.009
52. Niu Y, Xia S. Stroma – epithelium crosstalk in prostate cancer. *Asian J Androl*. 2009;11:28–35. doi:10.1038/aja.2008.39
53. Niu HJ, Zhang L, Feng JJ, Zhang QL, Huang H, Wang AJ. Graphene-encapsulated cobalt nanoparticles embedded in porous nitrogen-doped graphitic carbon nanosheets as efficient electrocatalysts for oxygen reduction reaction. *J Colloid Interface Sci*. 2019. doi:10.1016/j.jcis.2019.05.099
54. Niu HJ, Chen HY, Wen GL, Feng JJ, Zhang QL, Wang AJ. One-pot solvothermal synthesis of three-dimensional hollow PtCu alloyed dodecahedron nanoframes with excellent electrocatalytic performances for hydrogen evolution and oxygen reduction. *J Colloid Interface Sci*. 2019;539:525–532. doi:10.1016/j.jcis.2018.12.066
55. Chen HY, Jin MX, Zhang L, et al. One-pot aqueous synthesis of two-dimensional porous bimetallic PtPd alloyed nanosheets as highly active and durable electrocatalyst for boosting oxygen reduction and hydrogen evolution. *J Colloid Interface Sci*. 2019;543:1–8. doi:10.1016/j.jcis.2019.01.122